IPPI

Polyolefins Journal, Vol. 12, No. 4 (2025)
DOI: 10.22063/poj.2025.35771.1373
ORIGINAL PAPER

Optimizing carbon nanotube/polypropylene nanocomposites for enhanced conductivity and EMI shielding

Maziyar Sabet*

Chemical and Energy Engineering, Universiti Teknologi Brunei (UTB), Bandar Seri Begawan, Brunei Darussalam

Received: 13 September 2025, Accepted: 16 December 2025

ABSTRACT

Polypropylene (PP), a widely used polyolefin, suffers from poor electrical conductivity, which limits its use in electronic packaging and electromagnetic interference (EMI) shielding. In this study, conductive and EMI-shielding PP nanocomposites were fabricated using dual-functionalized carbon nanotubes (CNTs) via a solvent-free melt-blending route. Sequential acid and silane treatments improved CNT dispersion and interfacial compatibility, yielding a low percolation threshold of ~0.3 wt.% and an electrical conductivity of 1.2×10^{-2} S/m at 3 wt.% CNT. At 5 wt.%, the EMI shielding effectiveness exceeded 41.5 dB, with more than 80% of the attenuation arising from absorption, as confirmed by S-parameter analysis. AI-assisted image segmentation (U-Net architecture) quantified an ~80% reduction in CNT agglomeration and increased interparticle spacing, correlating with the enhanced electrical, dielectric, and thermal properties. The dielectric constant increased from ~2.3 in neat PP to ~6.0 at 5 wt.% CNT with low dielectric loss ($\tan \delta < 0.02$), while thermal conductivity improved by ~75%. Tensile strength and modulus increased up to 3 wt.% CNT with a moderate loss in ductility. The combination of dual CNT functionalization, scalable melt processing, and AI-based dispersion quantification provides a reproducible approach for designing lightweight, conductive, and EMI-shielding polyolefin nanocomposites for electronic, automotive, and aerospace applications. **Polyolefins J (2025) 12: 281-290**

Keywords: Polypropylene (PP); carbon nanotubes (CNTs); polyolefins; electrical conductivity; EMI shielding.

Highlights

- Percolation threshold of 0.3 wt.% was achieved with functionalized CNTs.
- EMI shielding >40 dB dominated by absorption.
- AI-assisted image analysis improved CNT dispersion reproducibility.
- Melt blending ensures solvent-free and scalable processing.

INTRODUCTION

Polypropylene (PP) is the most widely produced polyolefin and is used extensively in packaging, automotive components, and structural applications owing to its low density, chemical resistance, processability, and low cost [1-3]. However, its intrinsically insulating nature restricts its use in advanced applications such as electronic packaging and electromagnetic interference (EMI) shielding, where electrical conductivity, dielectric response, and thermal management are critical [4-6].

Carbon nanotubes (CNTs) are attractive nanofillers for imparting multifunctionality to polymers due to their high electrical conductivity, large aspect ratio, mechanical strength, and strong microwave attenuation capability [7-9]. When well dispersed, CNTs can transform PP into a lightweight, conductive material with useful EMI shielding performance while retaining thermoplastic processability [10-12]. Achieving this combination of properties at industrially relevant scales remains challenging.

*Corresponding Author - E-mail: maziyar.sabet@utb.edu.bn
maziyar_sabet@yahoo.com

The main difficulty lies in overcoming CNT agglomeration and ensuring strong CNT-PP interfacial adhesion. Van der Waals interactions, entanglement, and the mismatch between the graphitic CNT surface and nonpolar PP promote clustering and poor load transfer [13-15]. These issues increase the percolation threshold and degrade conductivity, dielectric performance, and shielding effectiveness [16-18]. Conventional approaches such as solvent casting, latex processing, or surfactant stabilization can improve dispersion but often lack scalability and raise environmental concerns [19,20]. Many reported systems still require relatively high CNT loadings (>6-8 wt.%) to achieve effective EMI shielding, which increases cost and can reduce toughness and processability [4-6].

Interfacial modification and advanced processing have therefore been widely explored. Previous works have used acid oxidation, silane coupling agents, or compatibilizers to improve CNT-polymer compatibility, and several studies have reported reduced percolation thresholds and improved EMI performance [10-12]. However, most of these reports either focus on functionalization without systematic EMI analysis or rely on qualitative microscopy to assess dispersion. Quantitative, reproducible links between nanoscale dispersion and macroscopic properties are still limited.

Recent advances in artificial intelligence (AI)-based image analysis offer a route to objective dispersion quantification. U-Net-type convolutional neural networks can segment microscopy images into filler-rich and polymer-rich regions, enabling extraction of dispersion metrics such as agglomerate area and interparticle spacing. When combined with well-designed experiments, such tools can support rigorous structure-property correlations and reduce operator bias.

In this work, we integrate dual CNT functionalization (acid and silane treatments) with solvent-free melt blending and AI-assisted image segmentation to develop conductive, EMI-shielding CNT/PP nanocomposites at low filler loadings. Compared with prior studies on CNT/polyolefin systems and AI-assisted dispersion analyses [10-12], the present work (i) achieves an ultra-low percolation threshold (~0.3 wt.%), (ii) demonstrates >40 dB EMI shielding dominated by absorption at only 5 wt.% CNT, and (iii) quantitatively links U-Net-derived dispersion metrics with electrical, dielectric, thermal, and mechanical responses. A comparative analysis with literature data is presented to highlight the incremental advances in performance and processing efficiency (Table 1).

This study therefore aims to: (i) design and fabricate CNT/PP nanocomposites using dual-functionalized CNTs via scalable melt blending, (ii) quantify CNT dispersion using an AI-based segmentation framework, and (iii) relate the resulting dispersion states to percolation behavior, EMI shielding mechanisms, dielectric properties, thermal conductivity, and mechanical performance.

EXPERIMENTAL

Materials

Isotactic polypropylene (PP; Moplen HP500N, melt flow index 2.5 g/10 min at 230°C/2.16 kg, LyondellBasell, Italy) was used as the matrix. Multi-walled carbon nanotubes (MWCNTs; outer diameter 10-20 nm, length 10-30 μm, purity >98%; CheapTubes Inc., USA) served as conductive fillers.

3-aminopropyltriethoxysilane (APTES, ≥99%, Sigma-Aldrich, Germany) as silane coupling agent was used for surface functionalization. Concentrated nitric acid (HNO_3, 65 wt.%) and sulfuric acid (H_2SO_4, 98 wt.%) were obtained from Merck (Germany) and used as received. Deionized water and absolute ethanol (Merck, Germany) were used for washing and silanization steps.

CNT Functionalization

CNTs were functionalized in two sequential steps. First, acid functionalization was performed using a 3:1 (v/v) mixture of concentrated H_2SO_4 (98 wt.%) and HNO_3 (65 wt.%). CNTs were dispersed in the acid mixture at a CNT:acid mass ratio of 1:20 and sonicated at 60°C for 4 h under reflux. The suspension was then

Table 1. Comparative performance of CNT-based composites for EMI shielding.

Study	CNT wt.%	Conductivity (S/m)	EMI Shielding (dB)	Fabrication Method	Reproducibility Method
Present Work	3	10^{-2}	>40	Melt blending + AI	AI segmentation (validated)
Ref [2]	5	10^{-3}	~35	Latex processing	Not reported
Ref [6]	8	10^{-2}	42	Solvent casting + metal	Manual SEM only
Ref [10]	6	10^{-4}	~30	Hybrid filler	Not discussed

diluted with deionized water, filtered, and repeatedly washed until neutral pH was reached, followed by vacuum drying at 80°C for 12 h. This treatment introduced carboxyl and hydroxyl groups (-COOH/-OH) on the CNT surface, improving wettability and providing reactive sites for silanization.

Second, silane functionalization was conducted by dispersing the acid-treated CNTs in ethanol containing 3 vol% APTES. The mixture was refluxed at 70°C for 3 h with mechanical stirring. After reaction, the suspension was filtered, washed with ethanol to remove unreacted silane, and dried at 80 °C. The APTES molecules were grafted onto the oxidized CNT surfaces, yielding amine-terminated, silane-functionalized CNTs designed to enhance interfacial bonding with the PP matrix during melt compounding.

Fourier transform infrared (FTIR) spectroscopy (Nicolet iS10, Thermo Fisher Scientific, USA) was used to verify the two-step functionalization (see Supporting Information, Figure S1). Compared with pristine CNTs, acid-treated CNTs exhibited a new band near ~1720 cm^{-1} (C=O stretching of -COOH), while silane-functionalized CNTs showed additional bands around ~1100 cm^{-1} (Si-O-Si) and ~1560 cm^{-1} (N–H bending), confirming the sequential introduction of oxygen-containing and silane groups.

Composite Fabrication

Dry-mixed blends of PP pellets and functionalized CNTs were prepared in a high-speed mixer and subsequently compounded using a co-rotating twin-screw extruder (LTE 26-44, Labtech Engineering, Thailand; screw diameter 26 mm, L/D = 44). The barrel temperature profile was set from 180 °C (feed zone) to 210°C (die), with a screw speed of 100 rpm. The screw configuration included kneading blocks to promote distributive and dispersive mixing.

The average residence time in the extruder was approximately 2.5 min, and torque was monitored to ensure stable processing. Under these conditions, the average shear rate in the main mixing zone was on the order of 200 s^{-1}, sufficient to break up agglomerates without severe CNT damage. Extrudates were water-cooled, pelletized, and compression-molded into plates using a hot press (Carver, USA) at 200°C and 10 MPa for 5 min, followed by cooling under pressure to room temperature.

CNT loadings of 0, 0.1, 0.3, 1, 3, and 5 wt.% were prepared to study percolation and multifunctional behavior. For EMI shielding and dielectric testing, circular specimens with thicknesses of 1.0 ± 0.05 mm were cut and thickness uniformity was verified using a digital micrometer at multiple locations.

Characterization

Morphology and dispersion

Field-emission scanning electron microscopy (FE-SEM; JSM-7001F, JEOL, Japan) and transmission electron microscopy (TEM; JEM-2100, JEOL, Japan) were used to examine CNT dispersion and morphology. For SEM, samples were cryo-fractured in liquid nitrogen, sputter-coated with a thin Au/Pd layer, and observed at 5-10 kV. For TEM, ultrathin sections (~70 nm) were prepared by cryo-ultramicrotomy and examined at 200 kV. No additional chemical staining or etching was applied; CNTs and crystalline PP regions were distinguished by their intrinsic contrast.

AI-assisted image segmentation

An AI-based image analysis pipeline was implemented using a U-Net convolutional neural network architecture. A dataset of 500 SEM/TEM image patches (512 × 512 pixels) was manually annotated to distinguish CNT-rich domains from the PP matrix. The dataset was divided into training/validation/test subsets of 70/15/15%. Data augmentation (random rotations, flips, brightness/contrast variations, and Gaussian noise) was used to improve generalization.

The model was trained with the Adam optimizer (initial learning rate 1×10^{-4}, batch size 8) for 100 epochs. Performance was evaluated using Dice similarity coefficient, intersection-over-union (IoU), precision, and recall. The final model achieved a Dice coefficient of 0.91 and an IoU of 0.85 on the test set, with precision and recall both above 0.90, indicating robust segmentation. Interparticle distance was computed as the mean shortest center-to-center distance between each CNT-rich domain and its nearest neighbour in the 2D projected plane, averaged over all domains and images. From the segmented masks, we also extracted quantitative metrics such as projected agglomerate area and interparticle spacing between CNT-rich domains.

Electrical conductivity

DC electrical conductivity was measured using a four-point probe setup (Keithley 2400 SourceMeter, Tektronix, USA) at room temperature. At least three independent specimens were tested for each composition, and average values with standard deviation (±SD) are reported; key average SD values, particularly around the percolation threshold, are

explicitly stated in the Results text.

EMI shielding measurements

EMI shielding effectiveness (SE) was evaluated in the X-band (8-12 GHz) using a vector network analyzer (E5071C, Keysight Technologies, USA) and a coaxial transmission-line fixture in accordance with ASTM D4935. The complex scattering parameters (S_{11}, S_{21}) were recorded and used to calculate total shielding effectiveness (SE_T) and its reflection (SE_R) and absorption (SE_A) components. Frequency-dependent plots of S-parameters, SE_T, SE_R, and SE_A are presented in the Results section.

Dielectric properties

Dielectric constant (ε') and dielectric loss (tan δ) were measured using an impedance analyzer (E4990A, Keysight Technologies, USA) over the frequency range 1 kHz– 1 MHz. Samples (diameter 20 mm, thickness 1.0 ± 0.05 mm) were coated with silver paste on both sides to form electrodes. Each measurement was repeated on three samples per composition.

Thermal conductivity

Thermal diffusivity was obtained using a laser flash analyzer (LFA 447, Netzsch, Germany). Thermal conductivity (κ) was calculated from $\kappa = \alpha \bullet \rho \bullet C_p$, where α is diffusivity, ρ is density (Archimedes method), and C_p is specific heat capacity. Three specimens per composition were tested and averaged.

Mechanical testing

Tensile properties were measured according to ASTM D638 using a universal testing machine (Instron 5567, Instron, USA) at a crosshead speed of 5 mm/min. Dog-bone specimens were cut from compression-molded plates. Stress–strain curves were recorded and used to obtain tensile strength, Young's modulus, and elongation at break (n = 5). Representative curves are provided to discuss deformation and failure mechanisms.

Theoretical Background: Percolation and EMI Shielding

The conductivity of CNT/PP composites above the percolation threshold can be described by the power-law relation:

$$\sigma = \sigma_0(\phi - \phi_c)^t \quad (1)$$

where σ is the electrical conductivity, σ_0 is a pre-factor, ϕ is the CNT volume fraction, ϕ_c is the percolation threshold, and t is the critical exponent. Fitting the experimental conductivity data to Eq. (1) (see Figure 1b) yielded $\phi_c \approx 0.3$ wt.% and the t value in the range typical for three-dimensional percolating networks.

For EMI shielding, the total shielding effectiveness (SE_T) is expressed as Eq. (2)

$$SE_T = SE_R + SE_A + SE_M \quad (2)$$

where SE_R is the contribution from reflection, SE_A from absorption, and SE_M from multiple reflections. These components were obtained from S_{11} and S_{21} following standard formulations. In conductive composites, absorption generally dominates due to dielectric loss, interfacial polarization, and ohmic dissipation.

The skin depth, δ, which characterizes the penetration distance of electromagnetic waves, is given by Eq. (3):

$$\delta = (\pi f \mu \sigma)^{-\frac{1}{2}} \quad (3)$$

where f is frequency, μ is the magnetic permeability, and σ is the electrical conductivity. Reduced skin depth at higher CNT content enhances absorption, thereby increasing SE_A and SE_T.

RESULTS AND DISCUSSION

Electrical Conductivity and Percolation Behavior

Figure 1a shows the electrical conductivity of CNT/PP composites as a function of CNT loading. Neat PP is insulating (~10^{-12} S/m), and conductivity remains low up to 0.1 wt.% CNT. A steep increase by about ten orders of magnitude is observed between 0.1 and 0.3 wt.%, reaching ~10^{-2} S/m at 0.3 wt.%, indicative of a percolation transition. Above 3 wt.%, conductivity tends to plateau, suggesting a saturated conductive network with reduced tunneling resistance.

Because error bars may appear faint after resizing and format conversion, key standard deviation values for the percolation regime are explicitly stated here in the text. To ensure that the reproducibility of the percolation transition is clearly documented, we report the average variability for the conductivity measurements around ϕ_c. For the 0.1-0.3 wt.% CNT range, the average standard deviation was approximately 9% of the mean conductivity values (n = 3). Across the full CNT-content range, the average standard deviation was approximately 7% of the mean values. These values support that the sharp

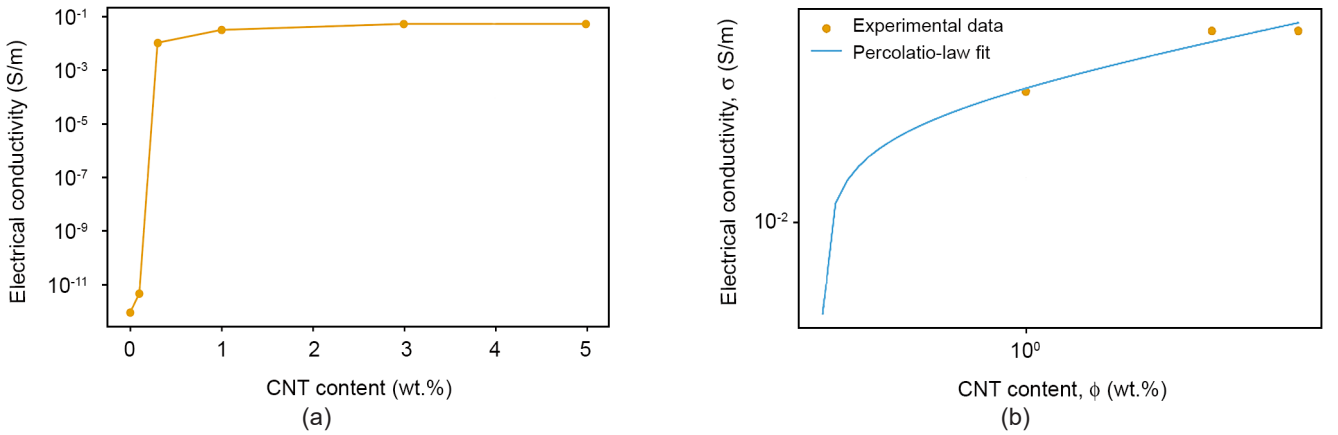

Figure 1. (a) Electrical conductivity of CNT/PP composites as a function of CNT content. (b) Percolation-law fit of electrical conductivity (σ) versus CNT content, ϕ, above the percolation threshold $\phi_c \approx 0.3$ wt.%, yielding a critical exponent t consistent with a three-dimensional percolated network.

conductivity jump at ϕ_c reflects a robust network-formation event rather than measurement scatter.

The conductivity data above the threshold were fitted to the percolation power law (Eq. (1)). The resulting fit (Figure 1b) yielded a percolation threshold $\phi_c \approx 0.3$ wt.% and a critical exponent t consistent with a three-dimensional, randomly distributed network. The low ϕ_c reflects the combined effect of dual CNT functionalization and efficient melt mixing, which promote network formation at low loadings.

Compared with literature data summarized in Table 1, the present system achieves similar or higher conductivity at significantly lower CNT contents than PP-based composites prepared by latex processing or sandwich structures [2,10,11]. These comparisons highlight the incremental advance of the current approach in reducing filler content while maintaining attractive electrical performance.

EMI Shielding Effectiveness and Mechanisms

The EMI shielding effectiveness (SE_T) in the X-band increased monotonically with CNT content. At 1 wt.%, SE_T was around 10 dB, suitable for partial attenuation. At 3 wt.%, SE_T exceeded 25 dB, and at 5 wt.%, SE_T surpassed 41.5 dB over most of the X-band, corresponding to more than 99.99% attenuation of the incident power. Figure 2a shows the frequency-dependent scattering parameters S_{11} and S_{21} for CNT/PP composites at representative CNT loadings in the 8–12 GHz range, while Figure 2b presents the corresponding total shielding effectiveness (SE_T) and its reflection (SE_R) and absorption (SE_A) components extracted from S_{11} and S_{21}.

Analysis of S-parameters and decomposition into SE_R and SE_A (Figure 2b) showed that absorption dominated the shielding behaviour. For the 5 wt.% composite, more than 80% of SE_T arose from SE_A across the X-band,

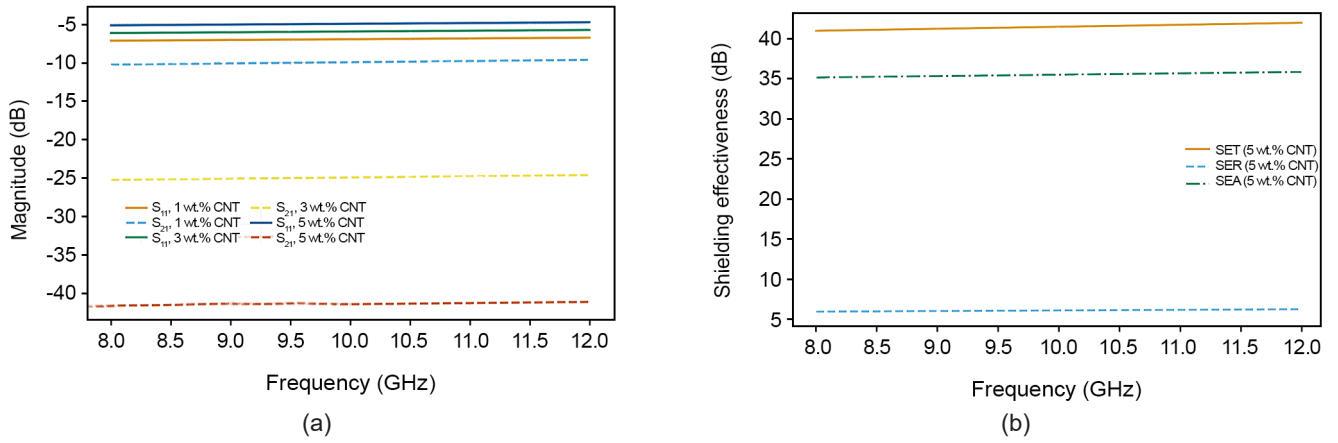

Figure 2. (a) Frequency-dependent scattering parameters S_{11} and S_{22} for CNT/PP composites with different CNT loadings in the X-band (8-12 GHz). (b) Corresponding total shielding effectiveness (SE_T) and its reflection (SE_R) and absorption (SE_A) components as a function of frequency, demonstrating absorption-dominated EMI shielding at higher CNT contents.

whereas SE_R contributed less, indicating adequate impedance matching between the composite and free space. The dominance of absorption is attributed to (i) multiple internal reflections within the percolated CNT network, (ii) dielectric loss associated with Maxwell–Wagner–Sillars interfacial polarization, and (iii) ohmic heating along conductive pathways.

When normalized by CNT content, the shielding per wt.% CNT compares favourably with hybrids and metal-assisted systems in similar frequency ranges (Table 1). Fu *et al.* [12] reported comparable EMI shielding at higher CNT loadings in sandwich-structured iPP/CNT foams, while Kaushal and Singh [10] required higher overall conductive filler contents to reach similar shielding levels. In contrast, the present CNT/PP nanocomposites achieve >40 dB absorption-dominated shielding at only 5 wt.% CNT, underscoring the effectiveness of dual functionalization and improved dispersion in reducing filler content while preserving strong EMI attenuation.

Dielectric Properties and Mechanistic Insights

Figure 3 presents the dielectric constant (ε') and dielectric loss (tan δ) as functions of CNT loading at a representative frequency. The dielectric constant increases from ~2.3 for neat PP to approximately 6.0 at 5 wt.% CNT. This enhancement arises from interfacial polarization and the formation of microcapacitor-like structures where conductive CNTs are separated by thin insulating PP layers.

Dielectric loss remained low (tan δ < 0.02) over the frequency range and did not increase sharply beyond the percolation threshold, indicating efficient polarization with limited dissipative loss. The steep rise in ε' around 0.3 wt.% coincides with the percolation threshold, consistent with the transition from isolated CNT clusters to a connected network that enhances interfacial polarization.

These characteristics—moderate permittivity, low loss, and tunability with CNT loading—are advantageous for applications requiring both EMI shielding and stable dielectric behavior, such as housings or components in electronic devices.

AI-Assisted Dispersion Quantification

The AI-based segmentation provided quantitative metrics for CNT dispersion that could be directly correlated with bulk properties. As summarized in the revised Table 2, at 2 wt.% CNT the optimized processing and functionalization reduced the projected agglomerate area by approximately 80% relative to

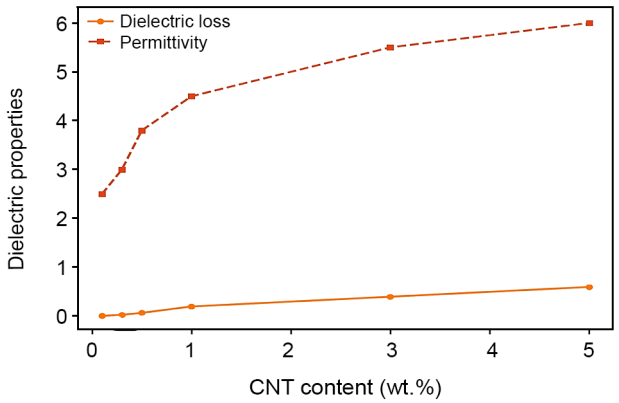

Figure 3. Dielectric constant (ε') and dielectric loss (tan δ) of CNT/PP composites with varying CNT loadings at a representative frequency. The sharp increase in ε' near percolation threshold is accompanied by low dielectric loss, supporting efficient interfacial polarization.

an initially mixed reference state at the same CNT loading, while the mean interparticle spacing between CNT-rich domains increased from ~70 nm to ~150 nm. To avoid ambiguity, the reduction in agglomeration is explicitly defined relative to this reference 2 wt.% CNT composite prepared without optimized conditions, rather than to neat PP, which does not contain CNTs and thus has no meaningful agglomerate metric.

The U-Net segmentation was validated against manual annotations on held-out images, yielding a Dice coefficient of 0.91, IoU of 0.85, and high precision/recall, confirming robust identification of CNT-rich regions. Representative raw and segmented images (Supporting Information, Figure S2) illustrate the improved dispersion, with fewer large clusters and a more homogeneous CNT distribution. These quantitative dispersion metrics correlate well with the observed low percolation threshold and improvements in electrical and EMI performance, underscoring the value of AI-assisted analysis for linking morphology to properties.

Thermal Conductivity and Phonon Transport

Thermal conductivity increased from 0.20 $W \cdot m^{-1} \cdot K^{-1}$ for neat PP to 0.35 $W \cdot m^{-1} \cdot K^{-1}$ at 5 wt.% CNT (Figure 4), corresponding to a ~75% improvement. Although the absolute numbers remain modest compared with metals or ceramic fillers, such an increase is significant for polyolefins and beneficial for dissipating heat in electronic packaging.

The improvement is governed by phonon transport along the CNT network and across CNT–PP interfaces. In the present composites, dual functionalization promotes better interfacial bonding, which can reduce

Table 2. AI-assisted dispersion metrics for CNT/PP composites at 2 wt.% CNT, comparing a non-optimized reference sample with the optimized composite. Agglomeration reduction is defined relative to the reference 2 wt.% sample.

Sample	Agglomerate Area (μm²)	Interparticle Distance (nm)	Agglomeration Reduction (%)
2 wt.% CNT (reference, no optimized functionalization/ processing)	4.2 ± 0.3	70 ± 5	0
2 wt.% CNT (optimized dual-functionalized CNT + optimized processing)	0.84 ± 0.07	150 ± 10	80

thermal boundary resistance and facilitate phonon transfer. However, several factors limit the magnitude of κ: (i) phonon scattering at CNT–PP interfaces, (ii) finite CNT aspect ratio and imperfect network continuity, and (iii) random orientation of CNTs, which precludes fully exploiting their high intrinsic axial conductivity. These limitations explain why the relative increase in κ is smaller than the improvements in electrical conductivity and highlight opportunities for further enhancements via hybrid fillers or alignment strategies.

Morphology and Failure Mechanisms

SEM and TEM images (Figure 5a,b) confirm reasonably uniform CNT dispersion and preservation of CNT morphology. Cryo-fractured SEM micrographs show CNTs embedded within the PP matrix with limited large-scale aggregation, consistent with the AI-derived agglomeration metrics. TEM images reveal well-defined tubular CNT structures embedded within partially crystalline PP regions. No evidence of severe CNT shortening was observed; most CNTs retained lengths in the micrometer range, suggesting that the sequential acid and silane treatments did not excessively damage the nanofillers under the chosen conditions.

Panels 5c–f present tensile fracture surfaces for neat PP and CNT/PP composites at representative loadings.

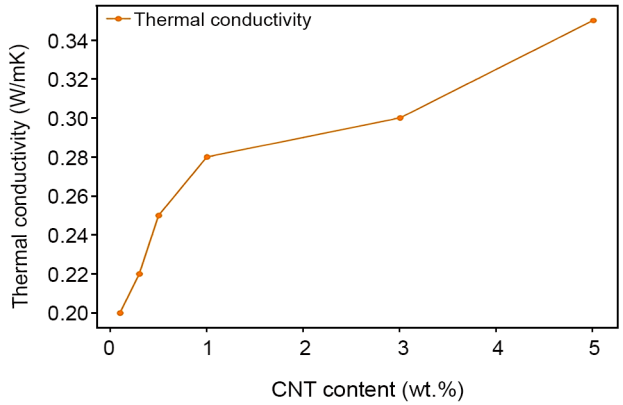

Figure 4. Thermal conductivity of CNT/PP composites as a function of CNT content, showing a ~75% increase at 5 wt.% CNT compared with neat PP.

In neat PP, the fracture surface is relatively smooth, indicative of ductile tearing with limited micro-cracking. At 1–3 wt.% CNT, the fracture surfaces become rougher and show clear evidence of crack bridging and CNT pull-out, indicating that CNTs contribute to load transfer and energy dissipation. At 5 wt.% CNT, more CNT bundles and localized fibrillation are visible, consistent with increased stress concentrations and matrix embrittlement at higher filler contents.

Although some CNTs appear locally straighter in the SEM micrographs, higher-magnification views and different fracture orientations reveal regions of waviness and entanglement. The apparent straightness arises in part from the 2D projection of a 3D network, the direction of cryo-fracture, and microtome sectioning for TEM. These factors can align or truncate individual CNTs in the viewing plane, but do not imply the absence of entangled or curved segments in the bulk.

The improved dispersion and interfacial adhesion can be rationalized by the dual functionalization strategy. Acid treatment introduces polar groups (–COOH/–OH) on the CNT surface, which subsequently react with APTES during silanization to form a thin silane-rich interphase. While PP itself is non-polar, the propyl segments of APTES provide an organic "bridge" that enhances wetting and physical entanglement with PP chains, reducing interfacial voids and improving load transfer. The combined effect is a more continuous CNT network with better mechanical coupling to the matrix, consistent with the observed increases in tensile strength and modulus at intermediate CNT loadings.

Mechanical properties of CNT/PP composites

Stress–strain curves and the corresponding mechanical parameters (Table 3) demonstrate that CNT addition up to 3 wt.% enhances tensile strength and modulus while moderately reducing ductility. At 3 wt.%, tensile strength and Young's modulus increased by ~18% and ~25%, respectively, compared with neat PP, whereas elongation at break decreased from ~450% to ~350%. This balance is desirable for structural applications where stiffness and strength are prioritized, but some

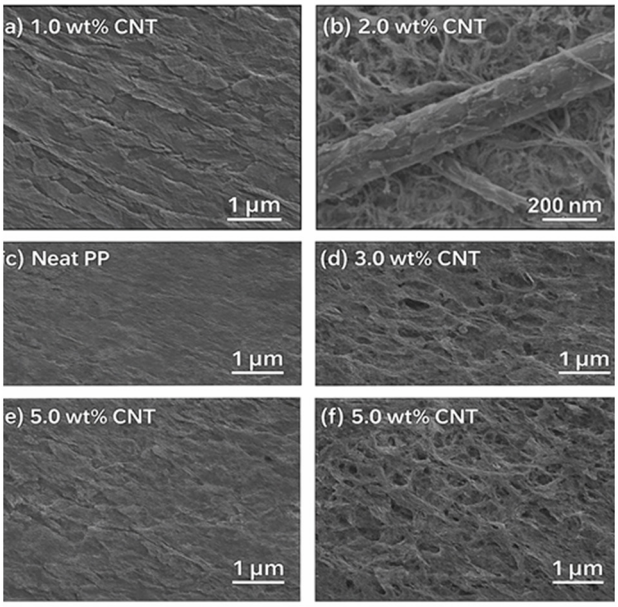

Figure 5. (a) SEM image of the CNT/PP composite with 1 wt% CNT, showing homogeneous dispersion within the PP matrix. (b) TEM image of the same composite, revealing well-preserved CNT morphology within partially crystalline PP regions (scale bar = 200 nm). (c,d) Tensile fracture surfaces of neat PP and 3 wt% CNT composites, illustrating the transition from smooth ductile tearing to rougher surfaces with CNT pull-out and crack bridging. (e,f) Fracture surfaces of the 5 wt% CNT composites captured from different regions at identical magnification (scale bar = 1 µm), showing pronounced CNT bundles and localized fibrillation. All panels include complete (a–f) labels.

ductility must be retained.

At 5 wt.% CNT, the elongation at break drops more sharply (~40% reduction relative to neat PP), despite a further increase in modulus. This behaviour is attributed to the formation of a more rigid, highly connected CNT network that constrains polymer chain mobility and promotes stress concentration sites at CNT clusters or imperfect interfaces. The higher probability of CNT–CNT contact and agglomeration at this loading reduces the capacity for plastic deformation and promotes brittle fracture.

Overall, the mechanical response is governed by competing effects of reinforcement and embrittlement: improved interfacial bonding and dispersion at 1-3 wt.% promote efficient load transfer, whereas increased network rigidity and local clustering at 5 wt.% compromise ductility. Finally, Figure 6 illustrates the integrated mechanism linking functionalization, dispersion, and network formation to the observed electrical, thermal, mechanical, and EMI-shielding behaviour.

Table 3. Mechanical properties of CNT/PP composites at different CNT loadings, including tensile strength, Young's modulus, and elongation-at-break.

CNT Content (wt.%)	Tensile Strength (MPa)	Young's Modulus (MPa)	Elongation-at-Break (%)
0 (Neat PP)	32.5 ± 0.9	1150 ± 50	450 ± 20
1	36.0 ± 1.1	1310 ± 45	410 ± 18
3	38.4 ± 0.8	1435 ± 52	350 ± 15
5	37.0 ± 0.9	1490 ± 60	270 ± 12

Challenges and future work

Although the present study demonstrates promising multifunctional performance in CNT/PP nanocomposites, several challenges remain for large-scale deployment. First, ensuring consistent dispersion and network formation in industrial extrusion lines is non-trivial. Variations in residence time, local shear fields, and temperature profiles can influence CNT alignment, percolation behavior, and final properties. Robust process windows, coupled with appropriate screw designs, must therefore be established and validated at pilot-scale.

Second, batch-to-batch variability in CNT feedstock, particularly in aspect ratio, surface chemistry, and impurity content—can affect both dispersion and percolation threshold. Standardized quality control protocols and tighter supplier specifications are needed to reduce such variability. At the same time,

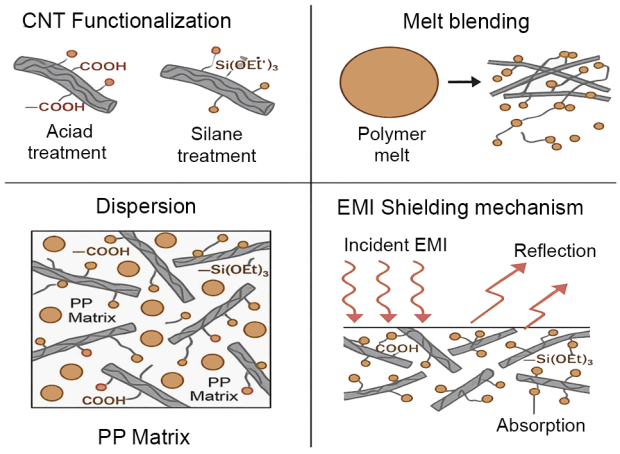

Figure 6. Schematic illustration of the integrated process: (i) acid treatment introduces oxygen-containing groups on CNT surfaces; (ii) subsequent APTES treatment deposits a thin silane-rich interphase; (iii) dual-functionalized CNTs are melt-blended into the PP matrix to form a well-dispersed, percolated network; (iv) the resulting network enhances charge transport, interfacial polarization, and absorption-dominated EMI shielding. Different graphical elements distinguish the oxidized CNT surface, salinized interphase, and surrounding PP matrix, highlighting the hierarchical structure of the composite.

excessive CNT loadings can compromise ductility and processability, emphasizing the importance of optimizing filler content and exploring hybrid filler combinations (e.g., graphene nanoplatelets or boron nitride) that could further enhance thermal or shielding properties at reduced total loading.

A third challenge lies in integrating AI-enabled dispersion monitoring directly into the processing line. While the present work uses AI-based segmentation as a post-processing tool, in-line sensing (optical, rheological, or thermal) combined with real-time AI analysis would enable adaptive, closed-loop control of dispersion and network formation.

Finally, environmental and safety aspects, including potential nanoparticle release and recyclability of CNT-reinforced PP, require systematic assessment. Understanding how CNTs affect existing PP recycling streams and developing safe handling and end-of-life strategies will be essential for sustainable industrial use.

Future work will therefore focus on: (i) scaling the processing protocol and defining robust process windows; (ii) investigating hybrid filler architectures; (iii) developing AI-assisted digital twins for real-time process control; and (iv) evaluating recyclability and life cycle impacts of CNT/PP systems.

CONCLUSION

This study demonstrates a solvent-free, scalable strategy for producing CNT/PP nanocomposites with enhanced electrical, dielectric, thermal, and EMI shielding properties at relatively low CNT loadings. Dual functionalization of CNTs via sequential acid and silane treatments, combined with co-rotating twin-screw extrusion, effectively mitigated CNT agglomeration and promoted network formation. The composites exhibited a low percolation threshold of ~0.3 wt.% and an electrical conductivity of 1.2×10^{-2} S/m at 3 wt.% CNT. At 5 wt.%, the EMI shielding effectiveness exceeded 41.5 dB in the X-band, with more than 80% of the attenuation arising from absorption. The dielectric constant increased from ~2.3 to ~6.0 while maintaining low dielectric loss ($\tan \delta < 0.02$), and thermal conductivity improved by ~75% compared with neat PP. Mechanical testing revealed simultaneous increases in tensile strength and modulus up to 3 wt.% CNT, with a moderate reduction in ductility.

A key aspect of this work is the integration of AI-assisted image segmentation to quantify CNT dispersion. U-Net–based analysis provided reproducible metrics for agglomerate area and interparticle spacing, which correlated with the observed percolation behavior and multifunctional performance. This approach offers a useful framework for establishing structure–property relationships in nanocomposites and can be extended to other polyolefin systems.

Taken together, these results indicate that dual-functionalized CNT/PP nanocomposites produced by melt blending are promising candidates for lightweight, conductive, and EMI-shielding components in electronic, automotive, and aerospace applications. Further optimization through hybrid fillers, process scaling, and AI-assisted process control is expected to broaden their technological impact.

DECLARATIONS

• Ethical Approval: Not applicable.
• Funding: None declared.
• Author Contributions: Maziyar Sabet conducted conceptualization, methodology, investigation, data analysis, writing, and supervision.
• Competing Interests: The author declares no competing interests.
• Data Availability: Available upon reasonable request.
• Supplementary Information: Additional FTIR spectra and representative AI-segmented morphology images are provided in the Supporting Information.
• Use of AI Tools: Generative AI tools were used only for language polishing (grammar and clarity) and formatting suggestions; all ideas, data analysis, and substantive scientific content are the author's own.

REFERENCES

1. Xu Z, Dou T, Wang YZ, Zuo H, Chen X, Zhang M, Zou L (2023) Three-dimensional printed carbon nanotube/polylactic acid composite for efficient electromagnetic interference shielding. Polymers 15: 3080
2. Xie Z, Chen H, Hu S, Zhao H, Chen W, Jiang D (2023) Graphene/carbon nanotube/polypyrrole composite films for electromagnetic interference shielding. Polym Compos 44: 3798-3807
3. Ghosh SK, Nath K, Nath Chowdhury S, Paul S, Ghosh T, Katheria A, Das P, Das NC (2023) Combination effect of functionalized high aspect

ratio carbonaceous nanofillers and carbon black on electrical, thermal conductivity, dielectric and EMI shielding behavior of co-continuous thermoplastic elastomeric blend composite films. Chem Eng J Adv 15: 100505
4. Kim YJ, Lee SC, Park HH, Jang KS, Lee SJ (2023) Electromagnetic interference shielding performance of poly(styrene-co-butyl acrylate)/carbon nanotube nanocomposites fabricated by latex technology. Ind Eng Chem Res 62: 5015-5023
5. Bleija M, Platnieks O, Macutkevič J, Banys J, Starkova O, Grase L, Gaidukovs S (2023) Poly(butylene succinate) hybrid multi-walled carbon nanotube/iron oxide nanocomposites: electromagnetic shielding and thermal properties. Polymers 15: 515
6. Wang Y, He Q, Gao YN, Yue T, Wang MC (2022) Achieving remarkable enhancement on electromagnetic shielding performance in multi-walled carbon nanotube/polydimethylsiloxane composites via adding a small amount of metal micro-particles as scattering points. Compos A-Appl S 162: 107135
7. Wu B, Qian G, Yan Y, Alam MM, Xia R, Qian J (2022) Design of interconnected carbon fiber thermal management composites with effective EMI shielding activity. ACS Appl Mater Interfaces 14: 49082-49093
8. He X, Feng L, Song H, Zhang J, Wei P, Jia X, Yang J, Li Y, Shao D, Wang S, Song Q (2022) Vertically aligned carbon nanotube@graphene paper/polydimethylsilane composites for electromagnetic interference shielding and flexible Joule heating. ACS Appl Nano Mater 5: 6365-6375.
9. Ghosh SK, Das TK, Ganguly S, Paul S, Nath K, Katheria A, Ghosh T, Nath C, Das NC (2022) Carbon nanotubes and carbon nanofibers based co-continuous thermoplastic elastomeric blend composites for efficient microwave shielding and thermal management. Compos A- Appl S 161: 107118
10. Kaushal A, Singh V (2022) Excellent electromagnetic interference shielding performance of polypropylene/carbon fiber/multiwalled carbon nanotube nanocomposites. Polym Compos 43: 3708-3715
11. Lin CL, Li JW, Chen YF, Chen JX, Cheng CC, Chiu CW (2022) Graphene nanoplatelet/multiwalled carbon nanotube/polypyrrole hybrid fillers in polyurethane nanohybrids with 3D conductive networks for EMI shielding. ACS Omega 7: 45697-45707
12. Fu L, Li K, Qin H, Hou J, Zhang X, He G, Liu B, Ren C, Chen J (2022) Sandwich structured iPP/CNTs nanocomposite foams with high electromagnetic interference shielding performance. Compos Sci Technol 220: 109297
13. Jang D, Yoon H, Seo J, Cho HJ, Kim GM, Kim YK, Yang B (2022) Improved electromagnetic interference shielding performances of carbon nanotube and carbonyl iron powder (CNT@CIP)-embedded polymeric composites. J Mater Res Technol 18: 1256-1266
14. Liu HX, Xu Y, Yang K, Yong H, Han D, Hong X, Yang Q (2023) Skin-like copper/carbon nanotubes/graphene composites and low thermogenesis during electromagnetic interference shielding. J Mater Chem C 11: 3010-3019
15. Wu S, Zhao Z, Hou H, Xue X (2021) EMI shielding nanocomposite laminates with high temperature resistance, hydrophobicity and anticorrosion properties. Nanomaterials 11: 3155
16. Mao Y, Xu L, Lin H, Li J, Yan DX, Zhong GJ, Li ZM (2022) Effective electromagnetic interference shielding properties of micro-truss structured CNT/epoxy composites fabricated based on visible light processing. Compos Sci Technol 227: 109296
17. Rengaswamy K, Asapu VK, Sundara R, Subramanian V (2022) Effective attenuation of electromagnetic waves by Ag adorned MWCNT-polybenzoxazine composites for EMI shielding application. Compos Sci Technol 223: 109411
18. Kallumottakkal M, Hussein MI, Haik Y, Abdul Latif T (2021) Functionalized-CNT polymer composite for microwave and electromagnetic shielding. Polymers 13: 3907
19. Yildirim F, Kabakçı E, Şaş HS, Eskizeybek V (2022) Multi-walled carbon nanotube grafted 3D spacer multi-scale composites for electromagnetic interference shielding. Polym Compos 43: 5690-5703
20. Kim YS, Lee JH, Park SJ (2021) Effect of ambient plasma treatment on single-walled carbon nanotubes-based epoxy/fabrics for improving fracture toughness and electromagnetic shielding effectiveness. Compos A-Appl S 148: 106456